PAPER

Effects of *in situ* dual ion beam (He^+ and D^+) irradiation with simultaneous pulsed heat loading on surface morphology evolution of tungsten–tantalum alloys

IOP Publishing | International Atomic Energy Agency Nuclear Fusion

Nucl. Fusion **58** (2018) 026016 (14pp) https://doi.org/10.1088/1741-4326/aa9e9b

Effects of *in situ* dual ion beam (He^+ and D^+) irradiation with simultaneous pulsed heat loading on surface morphology evolution of tungsten–tantalum alloys

S. Gonderman[a], J.K. Tripathi, G. Sinclair, T.J. Novakowski, T. Sizyuk and A. Hassanein

Center for materials under extreme environment (CMUXE), School of Nuclear Engineering Purdue University, West Lafayette, IN 47907, United States of America

E-mail: sean14@purdue.edu

Received 10 August 2017, revised 8 November 2017
Accepted for publication 1 December 2017
Published 22 December 2017

Abstract

The strong thermal and mechanical properties of tungsten (W) are well suited for the harsh fusion environment. However, increasing interest in using tungsten as plasma-facing components (PFCs) has revealed several key issues. These potential roadblocks necessitate more investigation of W and other alternative W based materials exposed to realistic fusion conditions. In this work, W and tungsten–tantalum (W–Ta) alloys were exposed to single (He^+) and dual ($He^+ + D^+$) ion irradiations with simultaneous pulsed heat loading to elucidate PFCs response under more realistic conditions. Laser only exposer revealed significantly more damage in W–Ta samples as compared to pure W samples. This was due to the difference in the mechanical properties of the two different materials. Further erosion studies were conducted to evaluate the material degradation due to transient heat loading in both the presence and absence of He^+ and/or D^+ ions. We concluded that erosion of PFC materials was significantly enhanced due to the presence of ion irradiation. This is important as it demonstrates that there are key synergistic effects resulting from more realistic fusion loading conditions that need to be considered when evaluating the response of plasma facing materials.

Keywords: plasma facing materials, tungsten, tantalum, fuzz, surface morphology, ion irradiation

(Some figures may appear in colour only in the online journal)

1. Introduction

Tungsten (W) has come to the forefront as plasma-facing components (PFCs) in fusion devices because of its strong thermal and mechanical properties [1–3]. Its high thermal conductivity (~170 W m^{-1} K^{-1} at room temperature) and melting point (~3700 K) combined with its low erosion under low-energy, high-flux ion bombardment make it well suited to withstand the extreme environment expected in the divertor region of future tokamak devices. However, despite these advantages, recent research has revealed W materials undergo extreme surface degradation when subjected to low energy helium (He) and deuterium (D) ion irradiation. This surface evolution manifests itself in the form of blister formation [4–6] and the growth of a nanostructure called 'fuzz' [7–9]. Due to the low energy of the incident ions, irradiation damage due to displacement cascades is limited and it is thought that the observed damage is due to the formation of bubbles [10–12] near the surface resulting from the large quantities

[a] Present address: General Atomics, San Diego, CA 92186, United States of America.

of implanted He and/or D. The final result is a PFC material surface driven far from equilibrium with substantially altered thermal [13, 14] and mechanical [15, 16] properties at the plasma surface interface.

In addition to large ion fluxes and steady-state heat loads expected in the divertor region, the presence of extreme transient heat loading events due to disruptions in the plasma are also expected [17–20]. The performance of candidate PFC materials exposed to single ion species (He or D) irradiation, and to a lesser extent, dual or sequential ion species (He/D) irradiation has been investigated extensively. However, very little work has been done in investigating the synergistic effects on surface modification when PFCs are exposed to dual ion (He^+ and D^+) irradiation with simultaneous pulsed heat loading to simulate transient events. This work is relevant to nuclear fusion applications, since transient heat loading during ion bombardment may significantly affect key PFC performance metrics, such as melting and cracking thresholds, erosion, and plasma contamination.

This study follows our previous reports where the synergistic effects of single versus dual ion irradiation on W and W–Ta alloy surface degradation were studied [21, 22]. In this work, an additional transient heat loading is applied using a Nd-YAG laser with millisecond (ms) duration to simulate transient heat loading events, i.e. edge-localized modes (ELMs) that are expected in future fusion devices [18, 20, 23–25]. Recent studies [20] designed to extrapolate the transient ELM events of current fusion experiments to that of ITER, suggest that divertor peak power flux during an ELM event will reach 1–10 GW m^{-2} and 10–200 MW m^{-2} in divertor region and main wall region respectively. Further experimental work [26] has shown that W PFCs already undergo cracking after 100 pulses with an energy density of 0.2 MJ m^{-2} and pulse duration of 500 μs (~0.4 GW m^{-2} power flux). This condition worsened when the energy density was increased to 1.5 MJ m^{-2} (~3 GW m^{-2} power flux) which resulted in formation of a melt layer that bridged the castellation of the sample structure. In addition to the surface deterioration due to melting or cracking, there is major concern that these transients may lead to significant erosion of PFC surfaces resulting in detrimental plasma contamination.

This issue was investigated in detail in another study [27]. The resulting experimental data showed the formation of crack networks propagating down into the material. The bifurcation of large cracks sometimes results in separation of small pieces of material, which are subjected to melting due to the decrease in thermal conductivity. This melting effect is also seen near crack edges where there a similar issue of insufficient heat conduction [27]. The study also showed that the melting threshold is around 0.55–0.57 MJ m^{-2}. This is explained by the formation of crack networks which decrease the thermal conductivity of the surface [27]. Melt material formed during the transients was redeposited downstream of the melt spot suggesting that plasma pressure gradient is a main force for the melt motion [28]. Other studies have looked at tracking the influx of eroded wall material by comparing the spectral lines for neutral and ionized W. The idea being that the inverse photon efficiency number for neutral W will not be affected by re-deposition [29]. Thus, any observed change in line intensity ratio can be described as a change in the prompt redeposited fraction. However, material loss analysis under transient conditions remains unclear and further investigation about melt layer behavior, damage conditions, and the resulting plasma impact is required.

Ongoing research using the Judith-I [30] and Judith-II [31] electron beam facilities have been testing PFC materials under transient thermal loads [32–37]. One study in particular [34] looked at the effect of high cycle ELM-like transients with steady-state heat loading. Similar to the conclusions discussed in [27], the results showed that prolonged exposure to pulsed heat loading (~10^6 pulses) results in cracking and damage on the surface below the expected damage threshold for W. In addition to these high cycle experiments, pulsed heat loading of W–Ta alloys was also investigated [33]. In those exposures, W–Ta samples exhibited resistance to crack formation and propagation when compared to pure W.

The experiments presented in this paper further investigate the response of W and W–Ta alloys to pulsed heat loading. Unlike the studies previously mentioned, the pulsed heat loading was simulated using a Nd:YAG laser system. In addition to the pulsed heat loading, W and W–Ta samples were also simultaneously exposed to single (He^+ ion) and dual ($He^+ + D^+$ ion) irradiation at elevated temperatures in order to enhance the deeper understanding the effect of the transient heat loading on the surface microstructure evolution and erosion in a more realistic fusion environment. Post ion- and laser-exposure analysis of samples was conducted using scanning electron microscopy (SEM), optical reflectivity and x-ray photoelectron spectroscopy (XPS) in order to correlate the damage and erosion on the sample surface to the exposure conditions.

2. Experimental methods

Three different W and W–Ta samples were investigated: one 99.95% pure W (from Alfa Aesar), and two W–Ta alloys having 1, and 5 wt.% of Ta (from American Elements). The W–Ta samples were sintered at 1500 °C and both the W and W–Ta powder had an average particle size of less than 10 μm. These samples will be denoted as W, W–1Ta and W–5Ta, respectively hereafter. The W and W–5Ta material was cut into 10 mm^2 samples that were 2 mm thick for experimental use. These samples were pre-characterized in a previous study [21] in order to confirm the Ta concentration in W–Ta alloys and their average grain size [22]. The use of electron backscatter diffraction (EBSD) and XPS have shown that the W and W–Ta samples had an average grain size of ~3–4 μm and were within 0.3% of their denoted wt.% composition. No preferential grain orientation was observed. Measuring the average grain size and grain orientation of the samples were necessary to ensure that all of the samples had similar grain features as pervious work [38–40] has shown these parameters to have an impact on surface damage in fusion environments. In order to better understand the synergistic damage effects caused by more complex heat loading conditions, three different sets of experiments were conducted.

2.1. Transient heat loading only experimental configuration

In order to generate the base case of damage accumulation due to transient heat loading, W, W–1Ta, and W–5Ta samples were exposed to a large number of transient heat loads at 1223 K. This temperature was maintained by using a button heater (resistive heater) with a thermocouple near the sample, and the elevated temperature (1223 K) was selected to simulate the expected surface temperature due to the anticipated steady-state heat loads. The resistive heater was equipped with a thermocouple-based feedback mechanism, i.e. a thermocouple imbedded in the back of the heater (touching the back of the sample) which is hooked up into a PID controller that adjusts heater filament current to compensate for any temperature changes. Surface temperatures during irradiation were also independently verified with radiation pyrometers (Ircon Modline 5 infrared sensor). Additionally, it is also important to mention that there are expected 'localized temperature spikes' due to the 'pulsed heat loading'. This transient enhancement in the temperature is one of the major mechanisms that might lead to damage of the surface; this will be discussed in detail in forthcoming sections. A pulse length of 1 ms, with a repetition rate of 1 Hz was selected to best represent the transient heat load, such as ELMs, expected in future fusion devices. The melt threshold for W has been reported to vary between 0.55–1.1 GW m^{-2} [13, 27, 41] depending on the parameters such as material grade, pulse frequency, and surface temperature. In the present study, a heat flux of 0.76 GW m^{-2} was chosen because it is within this range and is comparable to the heat flux magnitude, expected during an ELM-like transient event. This heat flux was then tested for high cycle loading of 3600 and 14 400 pulses to further investigate the impact of high cycle loading on the accumulated damage. The Nd:YAG laser system used for these experiments is a long pulsed, laser with a wavelength of 1064 nm, pulse width of 0.2–10 ms, and a repetition rate of 1–30 Hz. The maximum absorbed heat flux achievable with this system is ~2–3 GW m^{-2}. Before starting the experiments, the energy loss from the laser to the sample due to optical inefficiencies was calculated. This was done by comparing the energy being emitted directly out of the laser to the energy at the sample surface after passing through all the optics. A pyroelectric laser energy sensor was used to make this measurement, and it was found that ~32% of the energy was lost before reaching the sample. This measurement was weakly dependent on the energy of the laser, so multiple measurements were made at different energies (E) and an empirical formula for energy loss as a function of laser energy was calculated. This data has a strong linear trend. Applying least squares regression to the data, a linear approximation for laser energy loss based on pulse energy at the shutter was derived as: Energy loss (%) = 3.37 (E) + 29.32, where E is in joules (J). Using the energy loss relation and taking into account the optical reflectivity of the sample surface, the laser energy required to achieve certain absorbed heat flux conditions was determined. The pulsed heat flux from the laser was used in three main exposures types. First, laser only exposures were conducted for observing the damage induced on the PFC surface exclusively due to ELM-like transient heat loading. Second, He^+ ion irradiations with simultaneous and sequential ELM-like transient heat loadings were conducted to understand the impact of high flux He^+ ion irradiation on the laser induced damage. Finally, $He^+ + D^+$ ion irradiations with simultaneous and sequential ELM-like transient heat loadings were conducted to recognize the synergistic effects of high flux He^+ and D^+ ion irradiations on the laser induced damage. Figure 1(*a*) is a schematic of the experimental setup for the laser only exposures. For the laser only experiments, 1 ms pulses every second were used, to best simulate ELM-like transients. As mentioned previously, a heat flux of 0.76 GW m^{-2} was chosen because of its proximity to the melt threshold observed for W PFCs. It is important to note that there are still differences in the parameters being used in the present study that make a direct comparison to the cited literature [32, 33, 36, 41]. First, the heat fluxes in this study are being produced via Nd:YAG laser (as opposed to e-beam source, which were used in their studies [32, 33, 36, 41]). Second, our steady-state surface temperature is being maintained at 1223 K. This is to facilitate microstructure evolution when He^+ and D^+ ions are added in. These heat fluxes are then pulsed for 1 ms, every second, for 100 s (100 pulses), 1 h (3600 pulses) or 4 h (14 400 pulses) to understand the impact of high cycle loading PFC surface damage. As mentioned previously, laser only exposures were conducted first in order to provide the base cases, as a reference, for comparing the surface damage when He^+ and D^+ ions are introduced. Table 1 details the experimental conditions for each laser exposure.

2.2. He^+ ion irradiation with simultaneous transient heat loading experimental configuration

The next set of exposures utilize He^+ ion irradiation with pulsed heat loading. The focus of these experiments was to evaluate the effect of the additional ion bombardment on the surface damage induced during ELM-like transient heating events. In order to maintain directly comparable results, the same experimental configuration that was used for the laser only experiments was also used. The only difference being the use of the He^+ ion source. Figure 1(*b*) shows a schematic of the experimental layout. W and W–5Ta samples were exposed to 100 eV He^+ ion irradiation, with a flux of 6×10^{20} ions m^{-2} s, and surface temperature of 1223 K for 1 or 4 h with simultaneous pulsed heat loading from the laser.

Note, in addition to the simultaneous heat loading, these experiments were also repeated but in sequential order to compare the difference in damage induced by the laser after significant He^+ ion induced damage had already occurred. This was done by first irradiating with 100 eV He^+ ions, with a flux of 6×10^{20} ions m^{-2} s, and surface temperature of 1223 K for 1 h, followed by laser only pulsed heat loading for 1 h at 1223 K. Details of the exact experimental conditions for each sample is provided in table 1.

2.3. Dual ion ($He^+ + D^+$) irradiation with simultaneous heat loading experimental configuration

The set of experiments conducted for this paper are dual ion irradiations with simultaneous and sequential pulsed heat loading. These experiments mirror the layout of the laser only

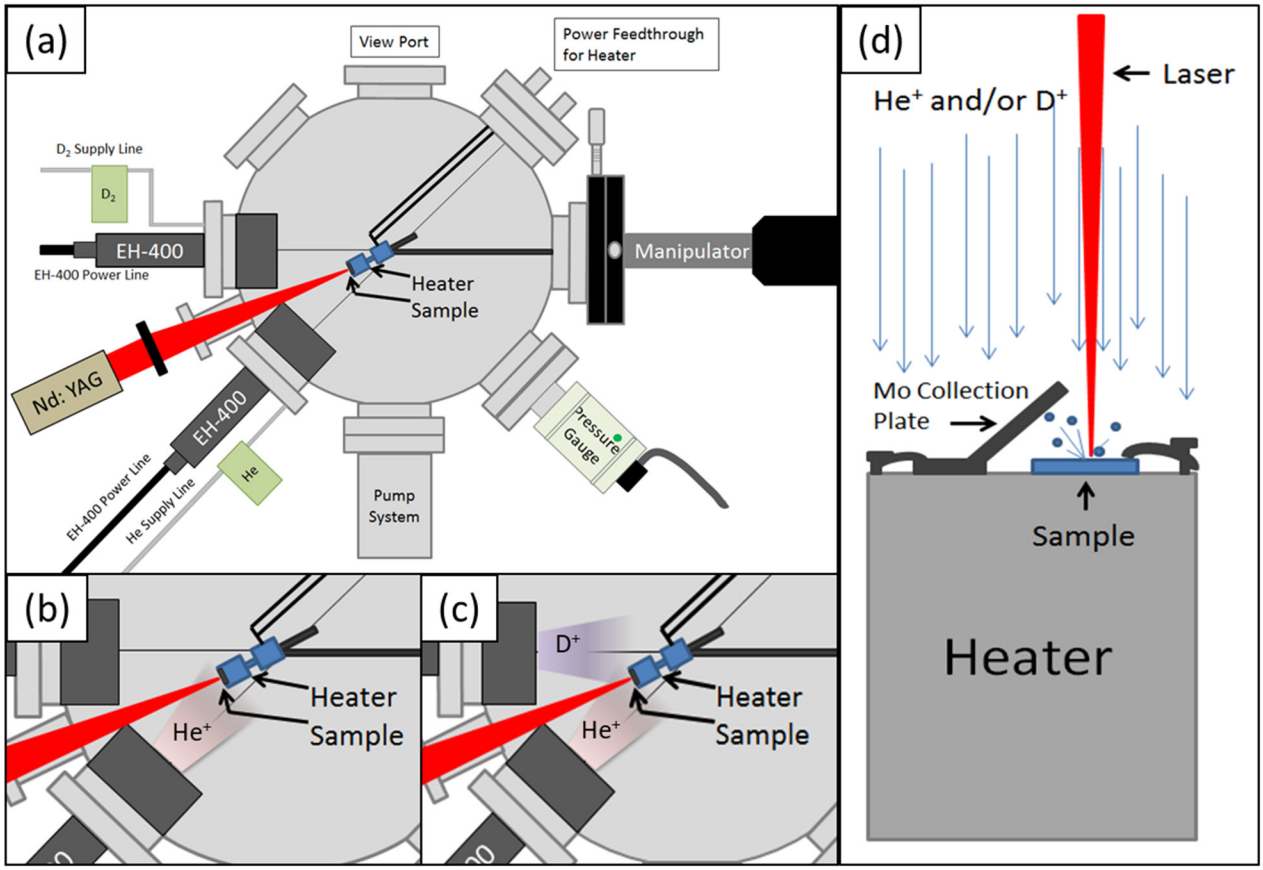

Figure 1. Schematic of the chamber configuration used for the (a) laser only exposures, (b) laser + He^+ ion exposures, and (c) the laser + He^+ ion + D^+ ion exposure. (d) Shows a more detailed schematic for the collection plate configuration used in the erosion experiments.

and He^+ + laser experiments but continue to add to the complexity by adding in the effect of D^+ ion irradiation. As such, the experimental setup is identical with the exception that the D^+ ion source is operated. A schematic of this layout is shown in figure 1(*c*). Note, due to simultaneous operation of both ion sources, some sacrifices in ion flux were made to increase stability during the ion irradiation. The fluxes were 3.0×10^{20} ion m^{-2} s for the He^+ ion source and 3.5×10^{20} ions m^{-2} s for the D^+ ion source. This resulted in a 46% He^+:54% D^+ ion ratio for the ion irradiation component of the exposure. In addition, to the simultaneous ion irradiation and ELM-like heat loading. This experiment was also performed sequentially as in the He + laser exposures. The specific details for each sample exposed to dual ion beam with simultaneous transient heat loading are provided in table 1.

2.4. Erosion studies experimental configuration

To find out the role of including the ion species on the erosion of the surface during transient heat loading, several additional experiments were pursued. This is achieved by the use of molybdenum (Mo) witness plates. These are essentially dummy samples placed at a 45° angle to sample's surface. The witness plates were positioned to maximize the collection of the eroded material while also shielding the collection surface from the ion irradiation. A schematic of the witness plate configuration is shown in figure 1(*d*). During ion irradiation the witness plate collected the eroded material from the sample surface. After then post irradiation XPS was performed on the witness plate to get quantitative analysis of the collect material. While the witness plate cannot provide explicit erosion measurements, it can be used to look at the relative difference in erosion from sample to sample. In this way, it is possible to make qualitative assessments of the magnitude of erosion relative to different samples and loading conditions. The exposure conditions for the samples used for erosion analysis are also provided in table 1.

3. Results and discussion

3.1. Laser only exposures

Several laser only experiments were conducted in order to provide a base from which to compare observed damage in the 'ion irradiation and laser' exposures. To do this, W, W–1Ta, and W–5Ta samples were exposed to pulsed heat loading with various heat fluxes and a steady state surface temperature of 1223 K. Figure 2 shows low magnification SEM images of W, W–1Ta, and W–5Ta samples exposed to 0.76 GW m^{-2} (0.76 MJ m^{-2} or 76 J cm^{-2}) heat for 1 or 4 h. This corresponds to 3600 or 14 400 pulses (1 ms pulse/second). We observed that with increasing the number of pulses there is a corresponding

Table 1. Exposure conditions for the laser only exposures, laser + He^+ ion exposures, laser + He^+ + D^+ ion exposures, and erosion experiments. WP stands for witness plate.

Sample ID	Number of pulses	Heat flux (GW m^{-2})	Pulse length (ms)	Frequency (Hz)	He Flux (ion m^{-2} s)	He fluence (ion m^{-2})	D flux (ion m^{-2} s)	D fluence (ion m^{-2})
Laser only								
W-1	3600	0.76	1	1	0	0	0	0
W-2	14400	0.76	1	1	0	0	0	0
W-3	100	0.76	1	1	0	0	0	0
W–1Ta-1	3600	0.76	1	1	0	0	0	0
W–1Ta-2	14400	0.76	1	1	0	0	0	0
W–5Ta-1	3600	0.76	1	1	0	0	0	0
W–5Ta-2	14400	0.76	1	1	0	0	0	0
W–5Ta-3	100	0.76	1	1	0	0	0	0
Laser + He^+ ions								
W-4	3600	0.76	1	1	6.00×10^{20}	2.16×10^{24}	0	0
W-5	14400	0.76	1	1	6.00×10^{20}	8.64×10^{24}	0	0
W-6 (He-then-laser)	3600	0.76	1	1	6.00×10^{20}	2.16×10^{24}	0	0
W–5Ta-4	3600	0.76	1	1	6.00×10^{20}	2.16×10^{24}	0	0
W–5Ta-5	14400	0.76	1	1	6.00×10^{20}	8.64×10^{24}	0	0
W–5Ta–6 (He-then-laser)	3600	0.76	1	1	6.00×10^{20}	2.16×10^{24}	0	0
Laser + He^+ + D^+ ions								
W-7	3600	0.76	1	1	3.00×10^{20}	1.08×10^{24}	3.50×10^{20}	1.26×10^{24}
W-8 (He + D then laser)	3600	0.76	1	1	3.00×10^{20}	1.08×10^{24}	3.50×10^{20}	1.26×10^{24}
W–5Ta-7	3600	0.76	1	1	3.00×10^{20}	1.08×10^{24}	3.50×10^{20}	1.26×10^{24}
W–5Ta-8 (He + D then laser)	3600	0.76	1	1	3.00×10^{20}	1.08×10^{24}	3.50×10^{20}	1.26×10^{24}
Erosion experiments								
W–WP-laser	1800	0.76	1	1	0	0	0	0
W–5Ta-WP-laser	1800	0.76	1	1	0	0	0	0
W–WP-laser + He	1800	0.76	1	1	6.00×10^{20}	1.08×10^{24}	0	0
W–WP-laser + He + D	1800	0.76	1	1	3.00×10^{20}	0.54×10^{24}	3.5×10^{20}	0.63×10^{24}

increase in the size of the damaged region. Also, the damage appears to be more severe. This is particularly noticeable in the W–Ta samples which exhibit larger cracks. This is intuitive as the larger number of transient events results in more energy being deposited and subsequently more damage due to the thermal cycling of the surface. The more interesting observation in the micrograph is the significant difference in performance between the W and W–Ta alloyed samples. For both the W–1Ta and W–5Ta samples large cracks and huge melt layers are observed. This is surprising as the relative concentration of Ta in these samples is low. Since Ta is miscible in W, it would be expected that the thermal and mechanical properties should scale according to Vegard's law [42]. Since the main damage mechanisms instigated via transient heat loading thermomechanical, it was expected that the performance between these samples would be similar. Even at a relatively low number of pulses the difference between the W and the W–Ta alloys is already noticeable. Figure 3 shows SEM micrographs for W and W–5Ta samples exposed to 100 pulses (0.76 GW m^{-2} energy) with a sample surface temperature of 1223 K (steady state).

As seen in figure 3, the damage for the lower number of pulses is consequently less severe in the pure W case. This is manifested in a smaller damaged region, but the onset of surface roughening caused by the thermal expansion and shrinking of grains is already apparent. Once again, the surface response in the W–5Ta sample is considerably more extreme. The appearance of cracks at even for such a low number of pulses helps to explain the large melted regions observed in the high cycle loading (figure 2). High cycle heat loading is speculated to induce micro-cracking over a large number of pulses [32]. This in turn can result in lowering the thermal conductivity of the near surface, resulting in melting at lower heat fluxes than expected. This may explain why melted regions are observed in the heavily cracked W–Ta alloys but not in the roughened pure W samples. Additionally, there was no significant difference between the W–1Ta and W–5Ta samples (figure 2) which implies that the accrued damage is not strongly dependent on Ta concentration. This suggests that other factors, such as material fabrication may be the reason behind the W–Ta alloy's poor thermal shock performance. In order to answer this question, Rockwell Hardness (RWH) testing was performed on both the W and W–5Ta samples. These measurements were made on pristine samples at room temperature. Table 2 shows the results of the measurements along with some other mechanical properties that were determined based on the RWH test.

The average hardness value and standard deviation was recorded for both the pure W and W–5Ta samples. In addition to the RWH measurement, a Brinell hardness number (BHN)

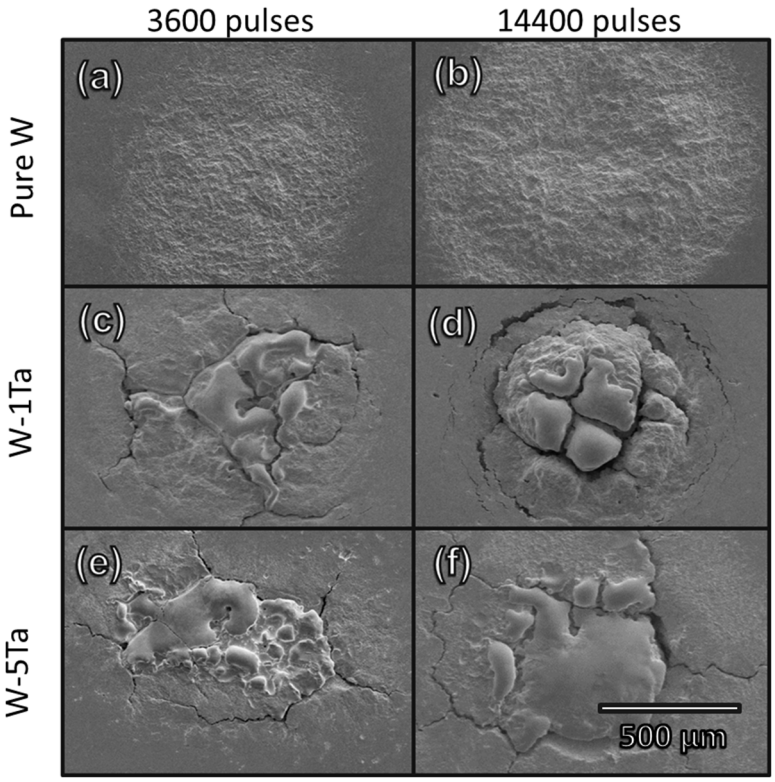

Figure 2. SEM micrographs of W, W–1Ta, and W–5Ta samples exposed to 3600 and 14 400, 0.76 GW m^{-2} pulses with surface temperature of 1223 K.

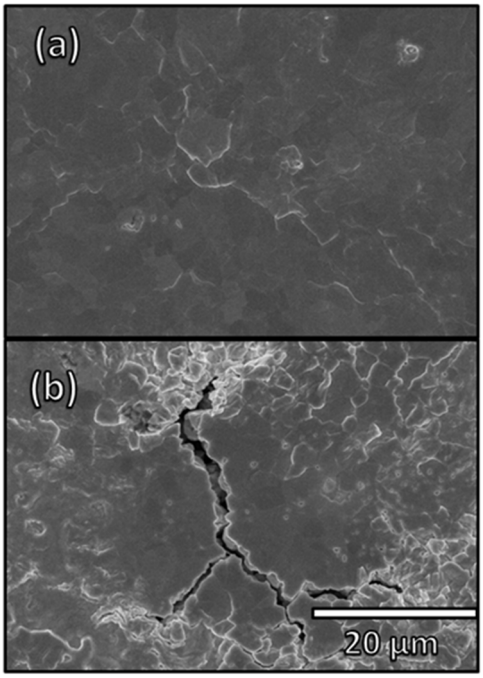

Figure 3. SEM micrographs of a pure W (a) and W–5Ta (b) samples exposed to 100, 0.76 GW m^{-2} pulses with surface temperature of 1223 K.

was calculated by measuring the diameter of the indented spot and using that to calculate the projected area of the indenter. Then dividing the force applied (981 N) by the projected area a hardness measurement was found. There were two main observations from this calculation. First, the average size of the indented area was larger for the W–5Ta samples when compared to the pure W samples. This implies that the W–Ta samples are less hard, and this is evident when the calculation is carried through to determine the hardness. It was found that the hardness for the pure W samples was 5.0 ± 0.9 GPa and the hardness for the W–5Ta samples was 3.6 ± 0.9 GPa. These values are consistent with the range of hardness values typical of W and W alloys [43]. Using a conversion chart from ASTM-E18 the ultimate tensile strength (UTS) of these materials from their RWH number was estimated [44]. Unsurprisingly, the W–5Ta samples have a lower UTS (500 ± 40 MPa) as compared to the pure W samples (640 ± 40). These differences in mechanical properties may be the reason that the W–Ta alloys perform poorly compared to the pure W samples. Under the intense heat loading, significant thermal stresses occur, and the weaker W–Ta samples are beginning to crack and melt while the pure W samples only exhibit surface roughening. These cracks compound the damage caused by the laser. The final result is substantially more thermally induced damage. The reason behind the difference in the mechanical properties

Table 2. Mechanical testing values and calculations made on W and W–5Ta samples.

Sample	W	W–5Ta
RW (B)	92 ± 2	81 ± 2
Indent dia (mm)	0.5 ± 0.1	0.6 ± 0.15
Projected area (mm^2)	0.20 ± 0.04	0.27 ± 0.06
BHN hardness (GPa)	5.0 ± 0.9	3.6 ± 0.9
Ultimate tensile strength (MPa)	640 ± 40	500 ± 40

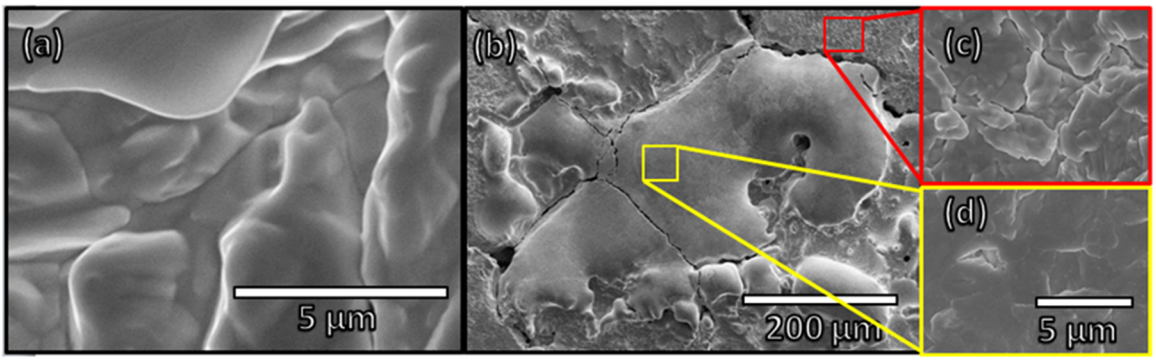

Figure 4. High resolution SEM micrograph a pure W sample exposed to 3600, 0.76 GW m^{-2} pulses with a surface temperature of 1223 K.

is likely due to the fabrication method of both samples because in an ideal alloy the thermomechanical properties should scale according to Vegard's law. This, combined with a recent study [33] on W–Ta alloys which showed better thermal shock performance of W–Ta alloys, suggest that the material fabrication process may be resulting in materials with significantly different properties.

Higher resolution SEM images of both the pure W and W–5Ta samples can be seen in figure 4. These micrographs provide insight into the small scale damage that is not visible in the low resolution images and provide a benchmark for comparison when the 'irradiation and transient heat loading' results are presented in the following sections.

Figure 4(*a*) shows the morphology that is characteristic for the entire damaged region in the pure W sample. The appearance of this shale-like structure is likely due to the enhanced surface diffusion and material motion induced by the transient heat loading events. The damaged region in the W–5Ta sample is more complex and exhibits several different morphologies in the damaged region. The top region, highlighted in figure 4(*c*), is located a few hundred μm from the center of the laser spot. In this region significant melt layer formation is not observed. Instead there is a shale-like structure similar to what was observed in the pure W samples. The bottom region in figure 4(*d*) is well within the large melt layer. While there are some large micron size cracks breaking up this region, most of the surface is relatively smooth. Higher resolution imaging (figure 4(*d*)), however, does indicate some roughening that could be the precursor for continued failure under further exposure.

3.2. He^+ ion irradiation with simultaneous and sequential pulsed heat loading

The next set of experiments focused on He^+ ion irradiation with simultaneous and sequential transient heat loading. Figures 5(*a*)–(*d*) is a set of SEM micrographs for a pure W sample exposed to He^+ ion irradiation (He^+ ion flux of 6×10^{20} ion m^{-2} s), with simultaneous 0.76 GW m^{-2} energy, 1 ms pulses/second for 1 h duration at 1223 K.

There was no obvious difference in the resulting morphology when comparing the sequential loading conditions and the laser only exposures. This is attributed to the large amount of thermally induced damage which essentially overwrites any pre-existing He induced damage. Even the difference in the simultaneous exposure is not apparent at low magnification where the damaged regions appears to be covered in a similar shale-like structure that was observed in the laser only exposures. As the magnification is increased, the appearance of pores in the simultaneous exposure is observed. In addition to the pores, the trenches and folds of the shale structure seem to be much deeper. This is particularly noticeable in figures 5(*c*) and (*d*). These deeper trenches may be the result of an increase in erosion due to the additional loading caused by the He^+ ions. This will be discussed further in the subsequent sections. For comparing the damage of the laser + He^+ ions to the damage only due to the low energy He^+ ions, SEM imaging was performed far away from the laser spot. Figure 5(*e*) shows the He^+ ion induced damage after 1 h of 100 eV He^+ ion irradiation at 1223 K on pure W. The lower flux results in a less developed fuzz surface, but the presence of pores and the formation of tendrils represents the early stage morphology of fuzz formation.

A similar effect is seen in the W–5Ta samples. Figures 6(*a*)–(*c*) shows SEM micrographs of a W–Ta sample exposed to 100 eV energy He^+ ions (He^+ ion flux of 6×10^{20} ion m^{-2} s) for 1 h at 1223 K followed by pulsed heat loading with a heat flux of 0.76 GW m^{-2}, with 1 ms pulses, every second for 1 h at a surface temperature of 1223 K. Once again the damage in the W–5Ta sample appeared to be more severe. This was expected due to the lower hardness and UTS of the W–5Ta samples compared to the pure W samples. Also, the sequential laser loading looked similar to the laser only results shown in figure 4. Similar to the pure W case, the shale-like structure that has been observed in the previous micrographs was still present and showed no evidence of previous He^+ ion loading. The main difference in the laser induced morphology caused by the pre-irradiation of the surface was the appearance of a grain-like structure in the melted regions. This microstructure is seen best in figures 6(*d*) and (*e*). These features are likely the result of recrystallization, but it remains unclear whether pronounced trenches or grain boundaries are the result of some sort of thermal grooving process or a feature of the He pre-irradiation.

Figure 7 is SEM micrographs of W–5Ta samples exposed to the same conditions detailed for figure 6, but for simultaneous loading. As in the pure W case, the simultaneous ion irradiation and transient heat loading of the W–5Ta samples

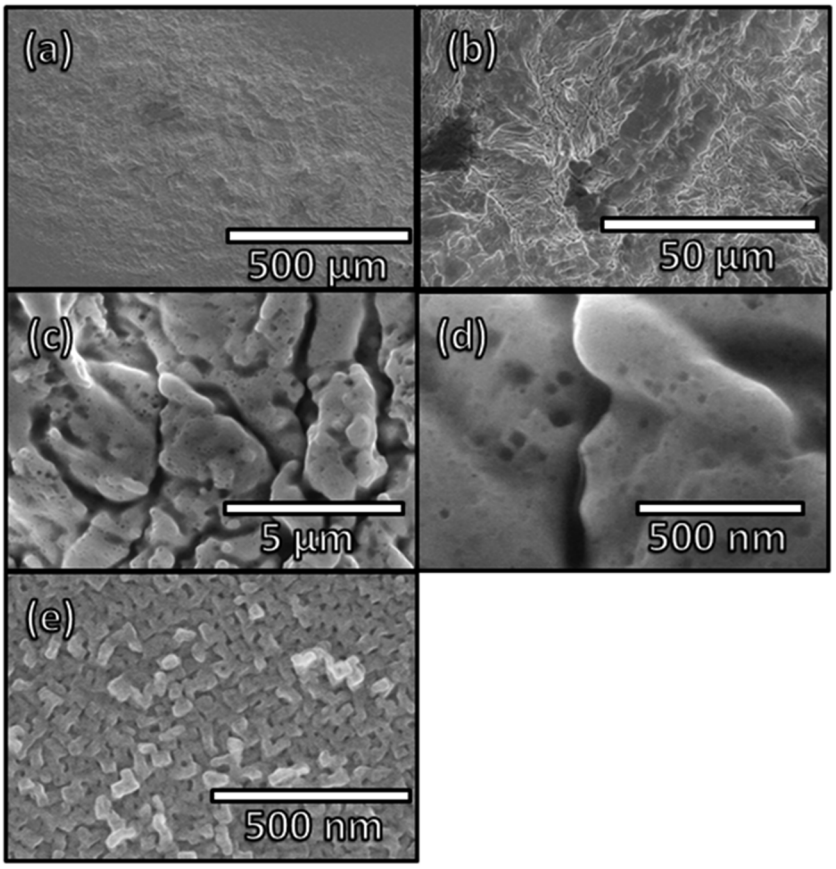

Figure 5. SEM micrographs ((a)–(d)) of a pure W sample exposed to 100 eV He^+ ion irradiation with simultaneous 0.76 GW m^{-2}, 1 ms pulses, every second for an hour at surface temperature of 1223 K. The flux of the He^+ ions was 6.0×10^{20} ion m^{-2} s. (e) is SEM micrograph of the same pure W sample taken far away from the laser irradiated region. The damage in this region is caused only by the 100 eV He^+ ions.

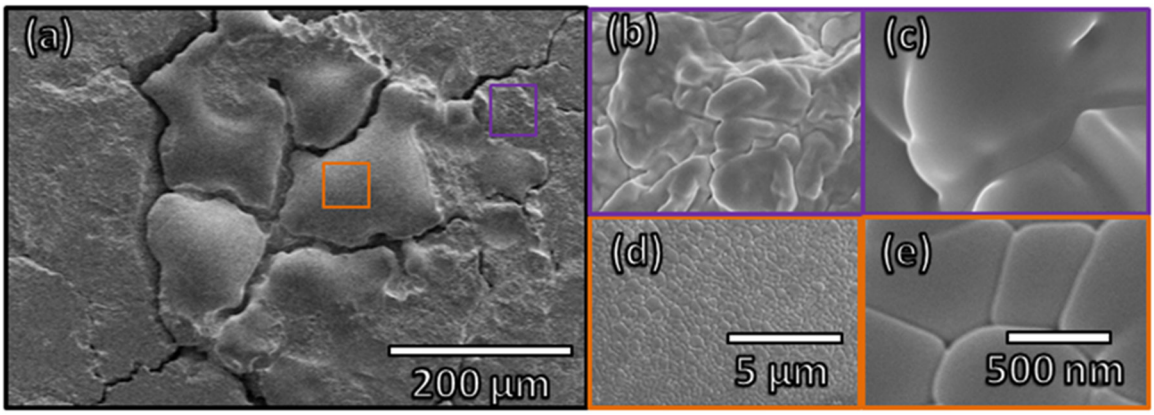

Figure 6. SEM micrographs of a W–5Ta sample first exposed to 100 eV He^+ ion irradiation followed by 0.76 GW m^{-2}, 1 ms pulses, every second for an hour at a surface temperature of 1223 K. The flux of the He^+ ions was 6.0×10^{20} ion m^{-2} s.

resulted in a significantly different microstructure. The shale-like structure previously discussed is still present, but the features seem more pronounced and the area is completely covered in pores. Additionally, figure 7(*c*) shows the melted region covered in the same grain microstructure from the sequential case. However, even these features have a slight difference. Figure 8 is high resolution SEM micrographs of the grain-like microstructure for the sequential and simultaneous exposures on W–5Ta samples, located in the large melted region. There is the presence of tiny pores in the SEM micrograph in figure 8(*b*). This is in contrast to the sequential loading case where no pores are observed. For comparing the damage regions of the laser to the damage only due to the low energy He^+ ion damage, SEM imaging was performed far away from the laser spots. Figure 8(*d*) shows the He^+ ion induced damage after 1 h of 100 eV He^+ ion irradiation at 1223 K on W–5Ta.

After looking at the difference in the microstructures during He^+ ion irradiation with sequential and simultaneous heat loading, there seems to be evidence of morphology

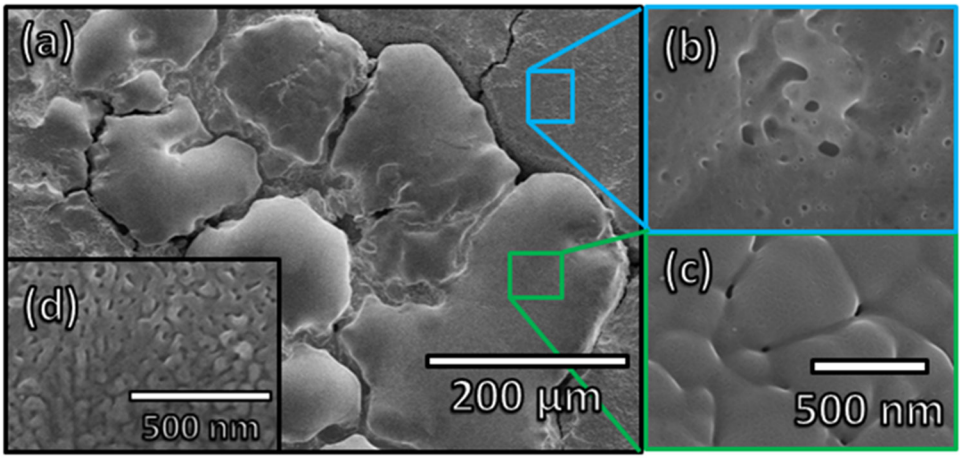

Figure 7. SEM micrographs ((a)–(c)) of W–5Ta sample exposed to 100 eV He^+ ion irradiation with simultaneous 0.76 GW m^{-2}, 1 ms pulses, every second for an hour at surface temperature of 1223 K. The flux of the He^+ ions was 6.0×10^{20} ion m^{-2} s. (d) is SEM micrograph of the same W–5Ta sample taken far away from the laser irradiated region. The damage in this region is caused only by the 100 eV He^+ ions.

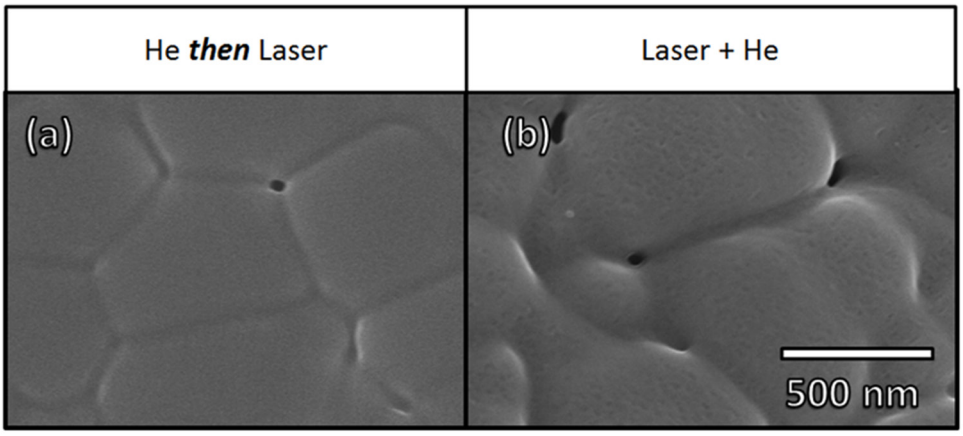

Figure 8. High resolution SEM of W–5Ta samples exposed to 100 eV He^+ ion irradiations at 1223 K with sequential (left) and simultaneous (right) heat flux loading of 0.76 GW m^{-2}, 1 ms pulses, every second for an hour.

differences in the laser induced damage caused by the presence of He. This issue presents itself in significant pore formation and deeper more extreme textures on the surface. These features may suggest enhanced erosion due to additional He effects during the transient heat loading.

3.3. Dual ion irradiation with simultaneous and sequential pulsed heat loading

The final set of experiments discussed in this paper investigate the synergistic effects on surface damage caused by dual ion ($He^+ + D^+$) irradiation with simultaneous transient heat loading on W and W–5Ta samples. He^+ and D^+ flux for these exposures were 3.0×10^{20} ion m^{-2} s and 3.5×10^{20} ion m^{-2} s, respectively. Figure 9 is comprised of SEM micrographs which detail the surface damage caused by 100 eV dual ion ($He^+ + D^+$) irradiation with simultaneous heat loading and a surface temperature of 1223 K. The heat flux used was 0.76 GW m^{-2}, with 1 ms pulses every second for an hour. Once again, the damage due to the laser resulted in a similar shale-like structure that has been seen in the previous transient heat loading conditions. Comparing the micrographs from figures 9(*c*) and (*d*) there are slight differences in the structure. This can be described predominantly by deeper trenches and the formation of pores in the shale-like structure. This behavior was also observed in the 'laser + He^+ ion' exposures, but its effect on key characteristics, like erosion, is unclear from the SEM micrographs.

Perhaps the most interesting difference in the material response is the significantly reduced number of pores in figure 9(*d*) as compared to figure 5(*d*). It was discussed in a previous study [22] that the presence of D^+ ion irradiation had a suppression effect on the He^+ ion induced damage. However, the manner in which that mechanism would interact with the pulsed heat loading remains unclear. It is possible the D^+ ion contribution is impacting the total amount of trapped gas in the near surface. This would manifest itself in fewer pores. In order to compare the damage region of the laser + simultaneous ($He^+ + D^+$) ion irradiation to the damage only due to the low energy $He^+ + D^+$ ion damage, SEM imaging was performed far away from the laser spot. Figure 9(*e*) shows the $He^+ + D^+$ ion induced damage after 1 h with a surface temperature of 1223 K on W.

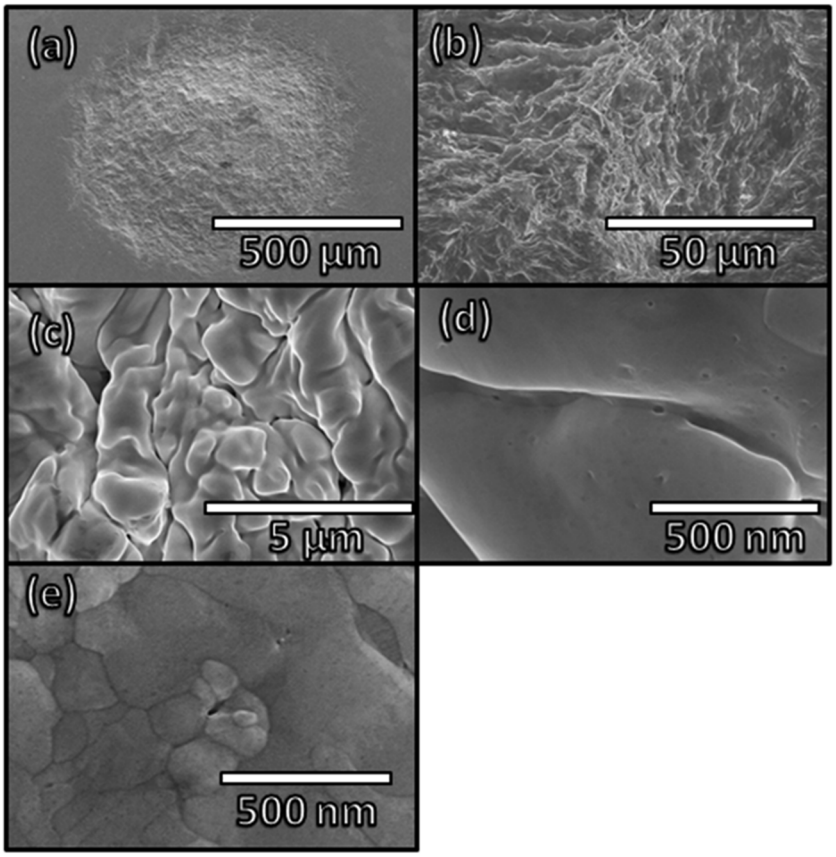

Figure 9. SEM micrographs ((a)–(d)) of a pure W sample exposed to 100 eV He^+ and D^+ ion irradiation with simultaneous 0.76 GW m^{-2}, 1 ms pulses, every second for an hour at surface temperature of 1223 K. The flux of the He^+ ions was 3.0×10^{20} ion m^{-2} s and the flux of the D^+ ions was 3.5×10^{20} ion m^{-2} s. (e) is SEM micrograph of the same pure W sample taken far away from the laser irradiated region. The damage in this region is caused only by the 100 eV He^+ and D^+ ions.

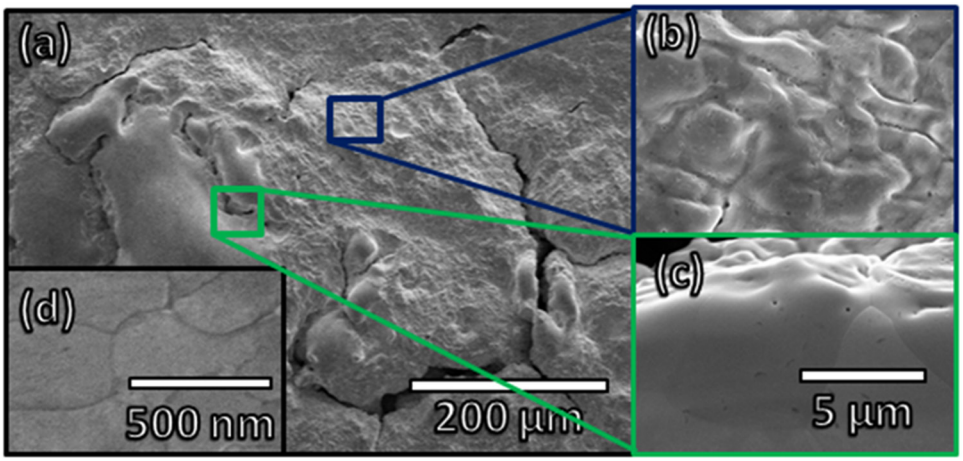

Figure 10. SEM micrographs ((a)–(c)) of a W–5Ta sample exposed to 100 eV He^+ and D^+ ion irradiation with simultaneous 0.76 GW m^{-2}, 1 ms pulses, every second for an hour at surface temperature of 1223 K. The flux of the He^+ ions was 3.0×10^{20} ion m^{-2} s and the flux of the D^+ ions was 3.5×10^{20} ion m^{-2} s. (d) is SEM micrograph of the same W–5Ta sample taken far away from the laser irradiated region. The damage in this region is caused only by the 100 eV He^+ and D^+ ions.

The surface morphology shown in figure 9(*e*) is consistent with trends observed in our previous study [22]. The addition of D^+ ions at high temperatures is suppressing the microstructure evolution on the surface. The same exposure conditions were applied to W–5Ta sample. Unsurprisingly, the W–5Ta sample responded in a similar manner to the pure W sample. The main exceptions being the large crack network formation and the corresponding melted region. These two differences were anticipated based on the results of laser only experiments, and are likely the result of weaker mechanical performance of the W–5Ta samples. Figure 10 is SEM micrographs of a W–5Ta sample exposed to simultaneous ($He^+ + D^+$) ion irradiation along with simultaneous pulsed heat loading with a heat flux of 0.76 GW m^{-2} for 1 h. Again, the sequential result

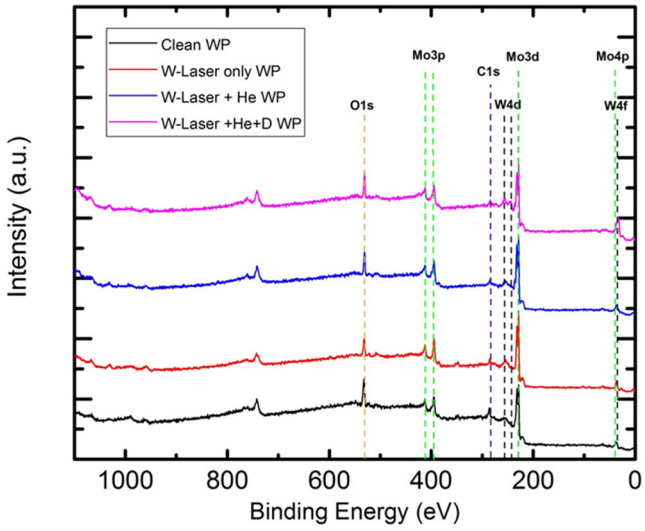

Figure 11. XPS wide scans for the different witness plate exposures for pure W samples.

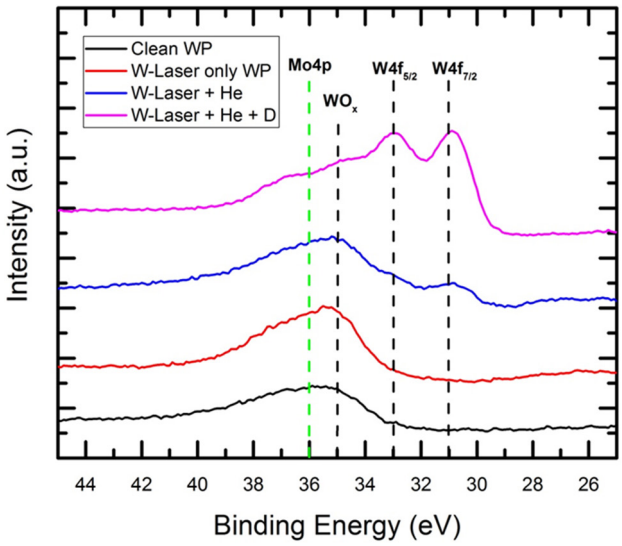

Figure 12. XPS region scans for the different witness plate exposures for pure W samples.

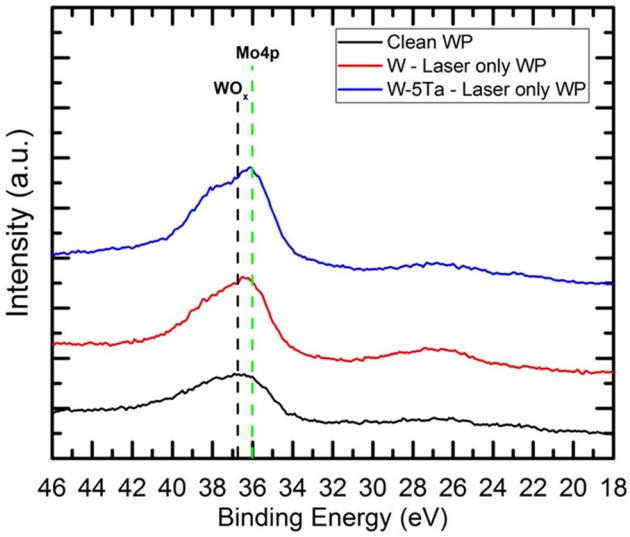

Figure 13. XPS region scan comparing the performance of pure W to W–5Ta samples under transient heat loading.

seemed to show little to no difference compared to the laser only experiments. It can be concluded that the heat flux used in these experiments exceeded the melt layer threshold regardless of whether the surface is pristine or pre-irradiated. The sequential laser loading is effectively erasing any evidence of surface damage in the pre-irradiation step.

As in the pure W case, figure 10(*c*) contains fewer pores when compared to its laser plus He^+ ion exposure counterpart. Again, this suggests a possible damage mitigation effect due to the presence of D^+ ions. For comparison purposes, the damaged region due to the 'low energy $He^+ + D^+$ ions' only, is provided in figure 10(*d*). SEM imaging was performed far away from the laser spot. Figure 10(*d*) shows the $He^+ + D^+$ ion induced damage after 1 h with a surface temperature of 1223 K on W–5Ta. Once again, the morphology is consistent with trends observed in our previous study [22]. The addition of D^+ ions at high temperatures is suppressing the microstructure evolution on the surface.

3.4. Erosion studies

The experimental conditions chosen for the erosion studies were based on our surface morphology findings as detailed in previous sections. The most interesting data was the difference in morphology due to the simultaneous heat loading and ion irradiation. Thus, in order to see the impact of these simultaneous exposures on the erosion of the surface, a witness plate exposure was conducted for the W samples exposed to laser only, 'laser + He^+ ions', and 'laser + He^+ ions + D^+ ions'. The specific details of transient-heat loading conditions are provided in table 1. Figure 11 depicts the survey XPS spectra of the Mo witness plates after each W exposure. Additionally, the figure also shows the survey spectra of a pristine Mo witness plate for the reference and comparison purposes. In addition to obvious Mo, C, and O XPS peaks, W peaks were observed as well. High resolution XPS spectra over the W_{4f} region was obtained to quantify the presence of W. Finally, the intensities of all XPS spectra were normalized for better comparison between spectra from different samples.

Figure 12 depicts the high resolution XPS region spectra of the witness plates after each W erosion experiments (including the pristine Mo witness plate, as a reference). Several interesting features were observed, firstly no evidence of W on the witness plate for the laser only exposure case and for the pristine Mo witness plate. These spectra are similar in shape and there is no detectable XPS peak where the W_{4f} peaks should be (~31 and 33 eV [45]). This is in contrast to our surface microscopy studies via FE-SEM (field emission scanning electron microscopy), where we observed extensive surface damage for the laser only exposers. It is possible that a longer exposure may be needed to collect enough material to see the XPS peaks. Also, it may be possible that the near proximity of the Mo_{4p} XPS peak is covering up the trace W signal. This is because the W_{4f} (W-oxide) XPS peaks are located very close

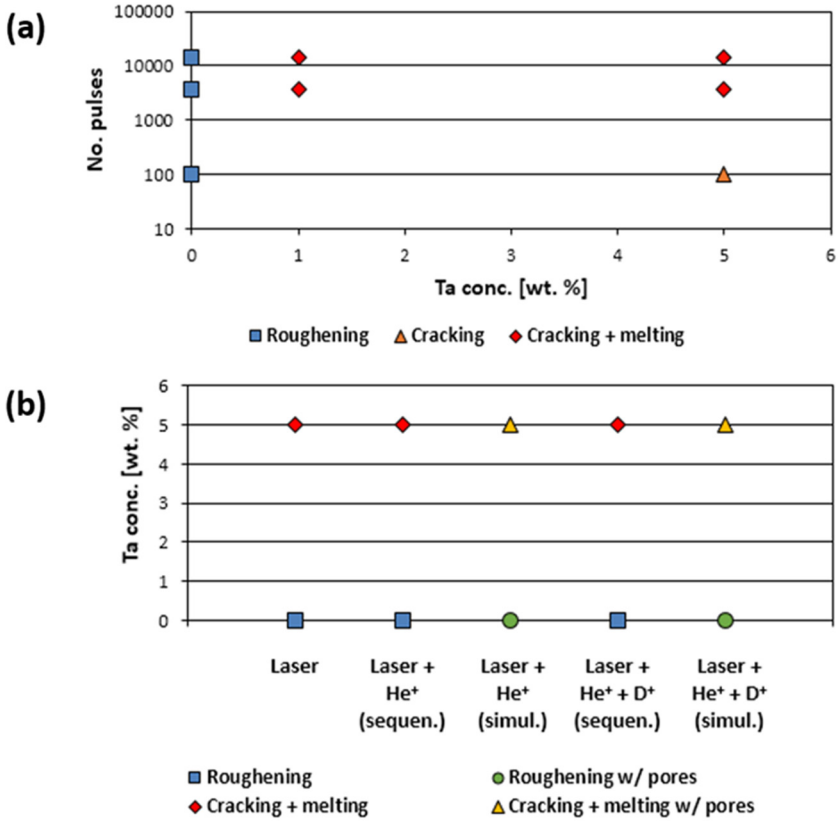

Figure 14. Summary of the findings from the present studies in different extreme conditions.

to the Mo_{4p} (~36 eV [44]). However, transient heat loading in presence of He^+ ion irradiation and dual ion ($He^+ + D^+$) irradiation causes significant evidence of W erosion on Mo witness plate (figure 12). It seems as if the presence of single ion (He^+) and/or dual ion ($He^+ + D^+$) irradiation during transient heat loading exacerbates the W erosion from the W surface. This observation corroborates the observations made from the surface morphology studies which suggested there may be evidence of increased erosion due to the deeper trenches and increased surface-porosity. Such significant enhancement in erosion may be due to the additional stresses resulting from the nucleation, growth, and diffusion of implanted gas species near the surface of W based PFCs. Note, selection of Mo as witness plate was due to the harsh radiation environment and the need for a material with low sputtering and a high melting temperature. Quantitative estimation of eroded W from the current spectra is extremely difficult since Mo_{4p} XPS peak is overleaping with W_{4f} (W-oxide) and so such calculations were not performed.

The same erosion study was also performed on W–5Ta sample under the same conditions and the results are presented in figure 13. As seen in figure 13, there is not a significant difference between the W and W–Ta samples. The peak counts are normalized to their respective Mo_{3d} peaks for comparison purposes, and there does seem to be a slight difference in the magnitude and shape of the peaks in figure 13 between the W and W–Ta region scans. However, this difference is right where the Mo_{4p} and the W_{4f} (W-oxide) peaks overlap. Based on the SEM micrographs, it was expected that W–Ta would result in more collected eroded material. This was because of the extensive damage observed. There are two possibilities that are being pursued to get more conclusive data for comparing the erosion performance of the pure W versus W–Ta samples. First, longer exposures with a more intense heat flux would result in more collected material and, therefore, a more easily differentiable set of data. Second, a background Mo subtraction algorithm could help see the presence of W even at low quantities. The second step seems to be more important during the identification of threshold for the onset of W-erosion.

4. Conclusions

Extensive surface morphological studies on W and W–Ta alloys as potential PFCs clearly revealed three major conclusions. First, a very apparent difference in the severity of the laser induced damage when comparing the W to the W–5Ta samples. This trend was consistent regardless of transient heat loading conditions. Mechanical properties measurements on W and W–5Ta samples show significant differences in both the hardness and UTS values. This suggests that the weaker W–5Ta samples fail more readily under the intense thermal stresses that are induced by the transient heat loading. Second, for the heat fluxes investigated in these experiments, there was essentially no difference in the resulting surface damage between the laser only exposures and the sequential ion irradiation followed by laser exposures. This is likely due to the fact that all of the tested heat fluxes were large enough to

effectively erase any pre-irradiation damage. Finally, the presence of ion irradiation (both single and dual) with simultaneous pulsed heat loading did show significant differences in the surface morphology. Deeper trenches and pore formation were observed, indicating for surface erosion enhancement. Such enhancement seems lower for dual ion irradiation case. This further supports our previous notion which states that the presence of D^+ ion irradiation at high temperatures may be working to mitigate some of the He induced damage. It was observed that the addition of single and dual ion irradiation greatly affected the amount of collected material on the Mo witness plate. This suggests that the presence of these ion species enhances the erosion of the PFC surfaces due to transient heat loading. Surface morphology observations indicate that the W–Ta samples would be undergoing significantly more erosion during the transient heat loading. A concise summary of the findings from these studies has been described in figure 14 as well for further detail.

Acknowledgment

This research was partially supported by National Science Foundation (Grant Number: 1243490-OISE) under the PIRE project.

ORCID iDs

T. Sizyuk https://orcid.org/0000-0003-0851-8632

References

[1] Davis J., Barabash V., Makhankov A., Plöchl L. and Slattery K. 1998 Assessment of tungsten for use in the ITER plasma facing components *J. Nucl. Mater.* **258–63** 308–12
[2] Bolt H., Barabash V., Federici G., Linke J., Loarte A., Roth J. and Sato K. 2002 Plasma facing and high heat flux materials—needs for ITER and beyond *J. Nucl. Mater.* **307–11** 43–52
[3] Federici G., Loarte A. and Strohmayer G. 2003 Assessment of erosion of the ITER divertor targets during type I ELMs *Plasma Phys. Control. Fusion* **45** 1523–47
[4] Gilliam S.B., Gidcumb S.M., Parikh N.R., Forsythe D.G., Patnaik B.K., Hunn J.D., Snead L.L. and Lamaze G.P. 2005 Retention and surface blistering of helium irradiated tungsten as a first wall material *J. Nucl. Mater.* **347** 289–97
[5] Ye M.Y., Kanehara H., Fukuta S., Ohno N. and Takamura S. 2003 Blister formation on tungsten surface under low energy and high flux hydrogen plasma irradiation in NAGDIS-I *J. Nucl. Mater.* **313–6** 72–6
[6] Venhaus T., Causey R., Doerner R. and Abeln T. 2001 Behavior of tungsten exposed to high fluences of low energy hydrogen isotopes *J. Nucl. Mater.* **290–3** 505–8
[7] Kajita S., Sakaguchi W., Ohno N., Yoshida N. and Saeki T. 2009 Formation process of tungsten nanostructure by the exposure to helium plasma under fusion relevant plasma conditions *Nucl. Fusion* **49** 095005
[8] Baldwin M.J. and Doerner R.P. 2010 Formation of helium induced nanostructure 'fuzz' on various tungsten grades *J. Nucl. Mater.* **404** 165–73
[9] Doerner R.P., Baldwin M.J. and Stangeby P.C. 2011 An equilibrium model for tungsten fuzz in an eroding plasma environment *Nucl. Fusion* **51** 043001
[10] Nishijima D., Ye M.Y., Ohno N. and Takamura S. 2004 Formation mechanism of bubbles and holes on tungsten surface with low-energy and high-flux helium plasma irradiation in NAGDIS-II *J. Nucl. Mater.* **329–33** 1029–33
[11] Sefta F., Hammond K.D., Juslin N. and Wirth B.D. 2013 Tungsten surface evolution by helium bubble nucleation, growth and rupture *Nucl. Fusion* **53** 073015
[12] Sharafat S., Takahashi A., Hu Q. and Ghoniem N.M. 2009 A description of bubble growth and gas release of helium implanted tungsten *J. Nucl. Mater.* **386–8** 900–3
[13] Kajita S., Takamura S., Ohno N., Nishijima D., Iwakiri H. and Yoshida N. 2007 Sub-ms laser pulse irradiation on tungsten target damaged by exposure to helium plasma *Nucl. Fusion* **47** 1358–66
[14] Nishijima D., Doerner R.P., Iwamoto D., Kikuchi Y., Miyamoto M., Nagata M., Sakuma I., Shoda K. and Ueda Y. 2013 Response of fuzzy tungsten surfaces to pulsed plasma bombardment *J. Nucl. Mater.* **434** 230–4
[15] Tokitani M., Kajita S., Masuzaki S., Hirahata Y., Ohno N. and Tanabe T. 2011 Exfoliation of the tungsten fibreform nanostructure by unipolar arcing in the LHD divertor plasma *Nucl. Fusion* **51** 102001
[16] Ueda Y., Coenen J.W., De Temmerman G., Doerner R.P., Linke J., Philipps V. and Tsitrone E. 2014 Research status and issues of tungsten plasma facing materials for ITER and beyond *Fusion Eng. Des.* **89** 901–6
[17] Pitts R.A. *et al* 2005 Material erosion and migration in tokamaks *Plasma Phys. Control. Fusion* **47** B303–22
[18] Zhitlukhin A., Klimov N., Landman I., Linke J., Loarte A. and Merola M. 2007 Effects of ELMs on ITER divertor armour materials *J. Nucl. Mater.* **365** 301–7
[19] Pitts R.A. *et al* 2013 A full tungsten divertor for ITER: physics issues and design status *J. Nucl. Mater.* **438** S48–56
[20] Loarte A. *et al* 2007 Transient heat loads in current fusion experiments, extrapolation to ITER and consequences for its operation *Phys. Scr.* **T128** 222–8
[21] Gonderman S., Tripathi J.K., Novakowski T.J., Sizyuk T. and Hassanein A. 2017 The effect of low energy helium ion irradiation on tungsten–tantalum (W–Ta) alloys under fusion relevant conditions *J. Nucl. Mater.* **491** 199
[22] Gonderman S., Tripathi J.K., Sizyuk T. and Hassanein A. 2017 Suppression of surface microstructure evolution in W and W–Ta alloys during simultaneous and sequential He and D ion irradiation in fusion relevant conditions *Nucl. Fusion* **57** 086001
[23] Federici G., Zhitlukhin A., Arkhipov N., Giniyatulin R. and Klimov N. 2005 Effects of ELMs and disruptions on ITER divertor armour materials *J. Nucl. Mater* **339** 684–90
[24] Leonard A.W., Herrmann A., Itami K., Lingertat J., Loarte A., Osborne T.H., Suttrop W., Modeling D. and Expert D. 1999 The impact of ELMs on the ITER divertor *Conf.: 13. Int. Conf. On Plasma Surface Interactions (San Diego, CA, United States, 18–22 May 1998) No. GA-A22860; CONF-980560* vol 269 pp 109–17
[25] Loarte A. *et al* 2003 Characteristics of type I ELM energy and particle losses in existing devices and their extrapolation to ITER *Plasma Phys. Control. Fusion* **45** 1549–69
[26] Wittlich K. *et al* 2009 Damage structure in divertor armor materials exposed to multiple ITER relevant ELM loads *Fusion Eng. Des.* **84** 1982–6
[27] Garkusha I.E. *et al* 2005 Tungsten erosion under plasma heat loads typical for ITER type I ELMs and disruptions *J. Nucl. Mater.* **337–9** 707–11
[28] Tereshin V.I., Garkusha I.E., Bandura A.N., Byrka O.V., Chebotarev V.V., Makhlaj V.A., Solyakov D.G. and

Wuerz H. 2003 Influence of plasma pressure gradient on melt layer macroscopic erosion of metal targets in disruption simulation experiments *J. Nucl. Mater.* **313–6** 685–9
[29] Van Rooij G.J. *et al* 2013 Tungsten divertor erosion in all metal devices: Lessons from the ITER like wall of JET *J. Nucl. Mater.* **438** S42–7
[30] Duwe R., Kühnlein W. and Munstermann H. 1994 The new electron beam facility for materials testing in hot cells-design and preliminary experience *Fusion Technology Proc.* **1** 22–6
[31] Majerus P., Duwe R., Hirai T., Winfried K., Linke J. and Rödig M. 2005 The new electron beam test facility JUDITH II for high heat flux experiments on plasma facing components *Fusion Eng. Des.* **79** 365–9
[32] Linke J. *et al* 2011 Performance of different tungsten grades under transient thermal loads *Nucl. Fusion* **51** 073017
[33] Wirtz M., Linke J., Pintsuk G., Singheiser L. and Uytdenhouwen I. 2011 Comparison of the thermal shock performance of different tungsten grades and the influence of microstructure on the damage behaviour *Phys. Scr.* **T145** 14058
[34] Loewenhoff T., Bürger A., Linke J., Pintsuk G., Schmidt A., Singheiser L. and Thomser C. 2011 Evolution of tungsten degradation under combined high cycle edge-localized mode and steady-state heat loads *Phys. Scr.* **T145** 014057
[35] Linke J., Escourbiac F., Mazul I.V., Nygren R., Rödig M., Schlosser J. and Suzuki S. 2007 High heat flux testing of plasma facing materials and components—Status and perspectives for ITER related activities *J. Nucl. Mater.* **367–70B** 1422–31
[36] Loewenhoff T., Linke J., Pintsuk G. and Thomser C. 2012 Tungsten and CFC degradation under combined high cycle transient and steady state heat loads *Fusion Eng. Des.* **87** 1201–5
[37] Spilker B., Linke J., Pintsuk G. and Wirtz M. 2016 Experimental study of ELM-like heat loading on beryllium under ITER operational conditions *Phys. Scr.* **T167** 014024
[38] El-Atwani O., Hinks J.A., Greaves G., Gonderman S., Qiu T., Efe M. and Allain J.P. 2014 *In situ* TEM observation of the response of ultrafine- and nanocrystalline-grained tungsten to extreme irradiation environments *Sci. Rep.* **4** 4716
[39] El-Atwani O., Gonderman S., Suslov S., Efe M., De Temmerman G., Morgan T., Bystrov K., Hattar K. and Allain J.P. 2015 Early stage damage of ultrafine-grained tungsten materials exposed to low energy helium ion irradiation *Fusion Eng. Des.* **93** 9–14
[40] El-Atwani O., Efe M., Heim B. and Allain J.P. 2013 Surface damage in ultrafine and multimodal grained tungsten materials induced by low energy helium irradiation *J. Nucl. Mater.* **434** 170–7
[41] Suslova A., El-Atwani O., Harilal S.S. and Hassanein A. 2015 Material ejection and surface morphology changes during transient heat loading of tungsten as plasma-facing component *Nucl. Fusion* **55** 33007
[42] Lubarda V.A. 2003 On the effective lattice parameter of binary alloys *Mech. Mater.* **35** 53–68
[43] Lassner E. and Schubert W.-D. 2012 *Tungsten: Properties, Chemistry, Technology of the Element, Alloys, and Chemical Compounds* (Berlin: Springer)
[44] Conversion chart from ASTM-E18: https://compass.astm.org/EDIT/html_annot.cgi?E18+17e1#s00094
[45] Moulder J.F., Chastain J. and King R.C. 2000 *Handbook of X-Ray Photoelectron Spectroscopy: a Reference Book of Standard Spectra for Identification and Interpretation of XPS Data* (Eden Prairie: Physical Electronics)